

## Improved Performance Prediction for Bo105 Model Rotor in Cruise Using Computational Fluid Dynamics

Joon W. Lim\*, Research Scientist  
Aeroflightdynamics Directorate (AMRDEC)  
US Army Research, Development and Engineering Command  
Ames Research Center, Moffett Field, California

An improvement in Bo105 model rotor performance prediction has been successfully made by coupling of unsteady and three-dimensional OVERFLOW 2 CFD aerodynamics solutions into CAMRAD II and using MSES-based table lookup in the CAMRAD II comprehensive analysis. Three approaches were used for performance prediction: CAMRAD II with the C81 table lookup, CAMRAD II with the MSES-based table lookup, and OVERFLOW-2/CAMRAD II coupling. The correlations were made with the Bo105 model rotor data in cruise for advance ratios of 0.06 to 0.34. The maximum prediction errors in a full sweep of speed were 16.8% for the C81, and 7.7% for the OVERFLOW, but the error was merely 3.3% for the MSES. The table lookup that was constructed at accurate Reynolds numbers as well as Mach numbers using MSES enabled the comprehensive analysis to significantly improve rotor performance prediction. Although it showed an excellent performance prediction, the CAMRAD II with the MSES-based table lookup was unable to capture the local characteristic of drag displayed by the OVERFLOW. This may be due to a lack of the adequate 3-dimensional aerodynamic capability in the comprehensive analysis.

### NOMEMCLATURE

$M^2_{c_c}$	nondimensional section chord force
$M^2_{c_d}$	nondimensional section drag
$M^2_{c_l}$	nondimensional section lift
$M^2_{c_m}$	nondimensional section pitching moment
$C_X$	Propulsive force coefficient, positive upstream
$C_{M_x}$	shaft roll moment, positive the right wing up
$C_{M_y}$	shaft pitch moment, positive the fuselage nose up
$C_P$	total power coefficient
$C_{P_i}$	induced power coefficient
$C_{P_o}$	profile power coefficient
$C_{P_p}$	parasite/climb power coefficient
$C_T$	thrust coefficient
$C_W$	weight coefficient
$c_{d0}$	zero angle of attack drag coefficient
$c_{d,min}$	minimum profile drag coefficient
$c_{l,max}$	maximum lift coefficient
$c_m$	pitching moment coefficient
$D_E$	equivalent rotor drag, newtons
$L$	rotor lift, newtons
$M$	Mach number
$n_{crit}$	critical amplification parameter in MSES
$R$	blade radius, m
$r$	blade span location, m

$\alpha$	angle of attack, degrees
$\alpha_s$	shaft angle, positive aft, degrees
$\sigma$	solidity
$\mu$	advance ratio

### INTRODUCTION

A Bo105 model rotor was tested for the cruise condition in the DNW facility using five different test sections with the intent to evaluate the influence of wind tunnel walls on measured rotor performance [1]. The five test sections included three closed sections, one open slot and one open jet. To ensure the accuracy of wind tunnel test methodology, validation studies were conducted using the model- and full-scale rotor wind tunnel tests as well as flight test [1-3]. These activities were conducted under the auspices of the US Army/German Memorandum of Understanding on Cooperative Research in the Field of Helicopter Aeromechanics, and concluded that the influence of wind tunnel wall induced interference on the performance could be compensated for by means of a shaft angle-of-attack correction.

The objective of the present paper is to address the current status of the cruise performance prediction capability for Bo105 model rotor and then to explore an improvement in performance prediction. The

---

\* lim@merlin.arc.nasa.gov

predictions are made using the CAMRAD II comprehensive analysis [4] as well as OVERFLOW-2/CAMRAD II coupled analysis [5]. In addition, rotor performance predictions are discussed in depth utilizing the MSES-based table lookup [6, 7] that is generated at accurate Reynolds numbers and Mach numbers.

## COMPUTATION MODELS

### Analysis Tools

Performance computations are made using a comprehensive code and CFD/CSD loose coupling. CAMRAD II [4] is a comprehensive as well as CSD code, and OVERFLOW-2 version 2.2 [8-9] is a CFD code.

For a structural model, the blade is discretized into sixteen nonlinear beam finite elements. The beam element is represented by three translational (axial, lead-lag, flap) and three corresponding rotational degrees-of-freedom (DOF), resulting in fifteen DOFs for each beam element. For an aerodynamic model, sixteen aerodynamic panels are defined. Steady airloads are computed using the lifting line theory with eight free wake trailers employed. The trim is set to satisfy measured target data (thrust, roll moment, and pitching moment) with trim variables of pitch collective, lateral cyclic, and longitudinal cyclic controls. A  $15^\circ$  time step is used in time integration.

The OVERFLOW-2 solution is computed on structured, overset grids having body-conforming near-body grids and Cartesian off-body grids. For time integration, the 1st-order implicit scheme is used with an azimuthal step of 0.05 degrees (7200 steps per cycle). For spatial discretization, the 5th-order Mapped Weighted Essentially Non-Oscillatory (WENOM) scheme is used [10].

A CFD/CSD loose coupling [5] is based on the strategy of replacing CSD airloads with CFD airloads, while rotor trim is achieved using CSD to account for blade deformation. The frequency of the airloads information exchange between the CFD and CSD codes is on a per-revolution basis.

### CFD Grids

The Bo105 model-scale rotor is a 40% Mach- and dynamically-scaled hingeless rotor. The rotor blade has a NACA 23012 airfoil section with a modified trailing edge tab, and the O-mesh topology is used in blade grid construction. The blade surface grid begins at

10cm from the hub center and covers to the blade tip. The near-body volume grid extends from the blade surface to approximately one chord length in the normal direction. Each blade grid system consists of blade grid, root cap and tip cap, and the dimensions of these grids are (295 x 89 x 53), (169 x 49 x 53), and (181 x 81 x 55), respectively. The rotor near-body grids include four sets of the blade grid, resulting in a total of 10.8 million grid points.

The rotor and fuselage surface grids are shown in Fig. 1 with a cut through the off-body volume grids. The fuselage grids consist of nine grids/patches including cap grids in the fuselage nose, the end of the sting and the top of the hub cylinder. And, the fuselage volume grid is made by extending from the surface grids to approximately one chord length in the normal direction, and the wall function,  $y^+$  is kept as unity for the first mesh from the surface. The fuselage near-body volume grid has a total of 0.7 million grid points

The near-body grids including a rotor and fuselage, have 11.5 million grid points - 10.8 million grid points for the rotor and 0.7 million for the fuselage. In the off-body grid, the level-1 finest mesh spacing is 0.10 chords, which totals 25.2 million grid points. Combining the near-body and off-body grids gives a total of 36 million grid points, and about 68% of these grid points belong to the off-body grid.

### NACA 23012 AIRFOIL

Most rotorcraft comprehensive codes use C81 table lookup [13] to simulate complex nonlinear blade aerodynamics in a lifting line theory. The C81 table provides steady lift, drag, and pitching moment for the 2-dimensional blade sections. The standard C81 format has two axes - Mach number and angle of attack - and Reynolds numbers are typically unavailable for the user.

The MSES code [6, 7] uses compressible Euler equations to solve for the inviscid flow field, coupled with suction and pressure solutions of a viscous boundary layer. The boundary layer transition location is determined via the amplitude ratio method ( $e^n$ ) using growth rates that are pre-computed from solutions of the Orr-Sommerfeld equation. The accurate critical amplification parameter,  $n_{crit}$ , can be empirically determined based on the measured data of the boundary layer transition and pressure for an airfoil. In this study, the standard value ( $n_{crit} = 9$ ) is used.

The C81 aerodynamic coefficients are presumably based on empiricism but can be alternatively computed using MSES code. The following section discusses the

2-dimensional aerodynamic coefficients computed using MSES against the existing C81 data.

### C81 vs. MSES Data

The Bo105 rotor blade consists of a constant airfoil section of NACA 23012. Reynolds numbers at  $M=1.0$  are  $6.34 \times 10^6$  for the full-scale rotor and  $2.78 \times 10^6$  for the model-scale. The tip Mach number is 0.64 for both rotors. The model-scale rotor blade has a 10% wider chord to match the maximum lift of the full-scale rotor [1].

The NACA 23012 C81 table, which was initially released from DLR and then slightly modified at AFDD [11], has been commonly used by researchers for HART II rotor simulation [12]. However, the actual Reynolds numbers are not specified in the C81 table. For this study, MSES data are generated at the adequate flow condition (Reynolds and Mach numbers) of the Bo105 model rotor, so as to construct a new MSES-based C81 table.

Figure 2 compares lift, drag, and pitching moment coefficients between the C81 table and the MSES data at  $M = 0.3, 0.5,$  and  $0.7$ . The lift computed using MSES agrees well with the C81 data, but for the drag and pitching moment two major differences are seen between the two data in: 1) minimum or zero-angle-of-attack profile drag ( $c_{d0}$ ), and 2) pitching moment slope,  $dc_m/d\alpha$ . Compared with the C81, the MSES  $c_{d0}$  is consistently lower for all Mach numbers, which will result in a lower power prediction. For example, at  $M=0.3$  the  $c_{d0}$  is 0.008 for the MSES and 0.010 for the C81, which indicates that the MSES  $c_{d0}$  is 20% lower than the C81. On the other hand, the pitching moment slope,  $dc_m/d\alpha$  from MSES is found positive at  $\alpha=0$ , while the C81 slope is about flat or slightly negative. It is worth noting that having a positive slope may induce blade aeroelastic instability.

Figure 3 shows the zero-angle-of-attack lift, drag, and pitching moment coefficients with Mach numbers. Over the C81 and MSES data, Boeing's C81 airfoil data is added. The Boeing data was the one that was used to evaluate the C81 rotorcraft flight simulation software [13]. It appears that there exists a resemblance between the C81 and Boeing data. However, the MSES data seems quite different. The MSES  $c_{d0}$  is significantly lower than the C81 data, and the difference gets even larger at higher Mach numbers. In fact, the MSES  $c_{d0}$  is lower than the C81 by 0.001 at  $M=0.2$ , but 0.003 at  $M=0.6$ . On the other hand, the MSES  $c_{m0}$  is slightly higher than the C81 data.

### Validation of MSES Data

A few measured data of NACA 23012 are used for validation of the MSES result. The University of Stuttgart data obtained by Althaus and Wortmann [14] was tested at a slow freestream speed in the University of Stuttgart wind tunnel. The Reynolds numbers ranged from  $0.75 \times 10^6$  to  $3.0 \times 10^6$ , and the corresponding Mach numbers were 0.03 to 0.13. Two airfoils were tested and their chord lengths were 0.5m and 1.0m. The Langley full-scale data (LaRC FS) reported by Jacobs and Smith [15] was tested at an even slower freestream speed in the NASA Langley's 30- by 60-foot full-scale wind tunnel. To match the desired Reynolds numbers, they used a very large airfoil section with a chord of 6 feet and a span of 36 feet. The Reynolds numbers ranged from  $1.6 \times 10^6$  to  $4.1 \times 10^6$ , and the Mach numbers were 0.04 to 0.10. Another NACA 23012 steady data reported by Loftin and Smith [16] was tested in the Langley 3- by 7.5-foot low turbulence (LaRC LT) wind tunnel. The Reynolds numbers ranged from  $0.7 \times 10^6$  to  $4.1 \times 10^6$ , and the Mach numbers ranged from 0.04 to 0.21.

The Mach numbers and minimum profile drag coefficients of these measured data are plotted in Figs. 4a-b. Since Reynolds number at  $M=1$  is  $2.78 \times 10^6$  for the Bo105 model rotor, the range of Reynolds numbers covered by the tests is sufficient, but their Mach numbers cover a significantly smaller region considering that Mach numbers in the C81 table is typically in the range of 0.2-1.0. In Fig. 4b, the effects of Reynolds number and Mach number are well displayed. The minimum drag decreases as Reynolds number increases, but it remains almost flat above the Reynolds number of  $2 \times 10^6$  to  $3 \times 10^6$ . The drag also decreases as Mach number increases.

Figures 4c-d show the correlation of the minimum drag coefficients by MSES for the University of Stuttgart and LaRC data, respectively. In Fig. 4c, the minimum drag coefficients are predicted reasonably, but the predictions do not show the Mach effect well which is found in the measured data. Figure 4d shows the correlation with the LaRC data. The MSES predicts well for the LaRC LT data, but shows a large discrepancy for the LaRC FS data. It is interesting noting that the drag in the LaRC FS data is significantly higher than the LaRC LT data. This high drag in the LaRC FS data would result primarily from a laminar separation bubble since the test condition was at very low Mach numbers, but it could be also related to the roughness of the airfoil surface or the technique of drag measurement.

**Table 1. Cases chosen from DNW test**

Case	Data point	$\mu$
L1	C2-598	0.06
L2	C2-594	0.09
L3	C2-602	0.14
L4	C2-618	0.17
L5	C2-614	0.23
L6	C2-610	0.28
L7	C2-606	0.32
L8	n/a	0.34

Figures 5-7 compare the drag polar between the C81 and MSES data with the measured data at Reynolds numbers of  $0.7 \times 10^6$ ,  $1.5 \times 10^6$ , and  $3.0 \times 10^6$ , respectively. Note that the target test condition is specified by the parenthesis in the legend for clarity, such as Stuttgart. As seen in Fig. 5a, at Reynolds number of  $0.7 \times 10^6$  the MSES prediction matches well the drag bucket of the Stuttgart data, but the  $c_{l,max}$  is over-predicted and approaches to the value of the C81 data. A large difference in the drag bucket region is found between the C81 and MSES data (see Fig. 5b). In fact,  $c_{d0}$  is 0.0102 for the C81 while it is 0.0081 for the MSES and 0.0078 for the Stuttgart data.

At Reynolds numbers of  $1.5 \times 10^6$  and  $3.0 \times 10^6$ , a large difference between the Stuttgart and LaRC FS (full-scale) data is seen in Figs. 6-7. This may be because a high drag exists in the LaRC FS data likely due to a laminar separation bubble. The MSES is unable to predict this high drag, which requires further investigation together with other CFD codes. For the Stuttgart drag data, the MSES prediction matches well.

The effects of Reynolds number and Mach number on drag polar are shown in Fig. 8. As described in Refs. [17-18], the increase in Reynolds number raises  $c_{l,max}$  at fixed Mach number and lowers  $c_{d,min}$  (see Fig. 8a). And, the increase in Mach number reduces  $c_{l,max}$  at fixed Reynolds number, and the  $c_{d,min}$  appears insensitive to this Mach range (see Fig. 8b).

Although the use of MSES helps to improve drag prediction, the slope of pitching moment ( $dc_m/d\alpha$ ) is predicted erroneously. In fact, for  $M=0.3$  the  $dc_m/d\alpha$  at  $\alpha=0$  degrees is 0.0006 by MSES, while the C81  $dc_m/d\alpha$  is -0.0004. It was found in Ref. [19] that the positive slope in pitching moment would result from the standard shape of the NACA 23012 trailing edge

tab which was used in the present MSES study. However, the current version of MSES exhibited a numerical difficulty with a modified trailing edge tab. Since the positive slope may cause instability of the blade, the MSES-based C81 table is made as a hybrid by keeping the lift and drag in the MSES data and replacing the pitching moment with the existing C81 data.

The final version of the MSES-based NACA 23012 airfoil table is generated by patching the existing C81 table with MSES data. The patched angle of attack is chosen in the range from -10 to 20 degrees or a subset of the range having MSES convergence, and the Mach numbers ( $M$ ) patched with MSES data are 0.2, 0.3, 0.4, 0.5, 0.6, and 0.7.

## DISCUSSION

### Experimental Data

For the task within the Memorandum of Understanding (MoU) between the US Army/NASA and the German DLR, a Bo105 model rotor was tested for the steady level flight conditions at  $C_w/\sigma = 0.07$  in the DNW wind tunnel [1]. For the model rotor, the tip Mach number is 0.64, and the Reynolds number at the tip Mach number is  $1.78 \times 10^6$ .

Figure 9 compares the power level ( $C_p/\sigma$ ) of Bo105 rotor for flight test, NASA AMES 40- by 80-foot full-scale test, and DNW model-scale test under the cruise condition [1-3]. The DNW data is obtained from the 40% Mach-scaled model rotor test in the 8x8m open test section of the DNW wind tunnel. The model-scale rotor has a 10% wider chord, and so its solidity is 0.077 while the full-scale rotor solidity is 0.070. The rotor shaft torque is used to determine the power. Table 1 lists the DNW test cases for advance ratios from 0.06 to 0.34. Although the highest speed case (L8) is not a part of the DNW test, it is included for this study and the associated trim targets are estimated through the curve-fitting of the DNW data.

Figures 10a-b show the levels of measured thrust ( $C_T/\sigma$ ), shaft roll moment ( $C_{MX}/\sigma$ ), and pitching moment ( $C_{MY}/\sigma$ ) in the DNW test. These values are used for trim targets with the trim variables selected as the pitch collective, lateral, and longitudinal cyclic controls. Note that the roll moment is defined positive for the right wing up, and the pitching moment is positive for the fuselage nose up. For the purpose of smoothing as well as extrapolation of these data, a polynomial is used, and their polynomial expressions are given in the figure. Shaft angles (positive aft)

before and after wall correction is shown in Fig. 10c, where the Glauert wall correction for the open section is applied [1].

### Rotor Performance Correlation

Performance prediction for a Bo105 model rotor is made using three approaches: 1) CAMRAD II comprehensive analysis using the existing C81 table lookup (C81), 2) CAMRAD II comprehensive analysis using the MSES-based table lookup (MSES), and 3) OVERFLOW-2/CAMRAD II coupled analysis (O2/CII).

In the CFD/CSD coupling process, blade force and moment are not fully conserved, which would result from various factors: 1) difference in the surface resolution between the CSD aerodynamic computation surface (low resolution) and the CFD blade surface grid (high resolution), 2) difference in the order of numerical integration scheme in the CSD and CFD airloads computation, 3) inconsistency in the blade geometry between the CSD and CFD input, or 4) difference in the lifting surface area for the CSD and CFD airloads. Reference [20] reported for the UH-60A rotor that there was an averaged difference of 2 to 2.5% in thrust between the CFD and CSD result.

A thrust comparison is made for the Bo105 model rotor at DNW. Figure 11a compares the thrust level ( $C_T/\sigma$ ) between the CSD (CAMRAD II) and CFD (OVERFLOW 2). The CSD lifting surface area is defined typically from the blade root cutout to the tip - in this study,  $r/R=0.22-1.0$  - while the CFD lifting surface area includes the CSD lifting surface area plus the region from the shank to the root cutout ( $r/R=0.05-0.22$ ). The difference between the CSD and CFD  $C_T/\sigma$  is shown. The CSD  $C_T/\sigma$  is lower by 1.4 to 2.4% than the CFD  $C_T/\sigma$  (see Fig. 11b), which is seen similarly in Ref. [20]. However, the CFD  $C_T/\sigma$  without having the shank area (CFD-Shank) differs only by 0.8% or less from the CSD, which indicates that the shank area is mainly responsible for the unbalanced  $C_T/\sigma$  between the CFD and CSD. Note that the imbalance in  $C_T/\sigma$  would be less in a real blade since the shank geometry is not accurately modeled in the OVERFLOW grid.

The power level ( $C_P/\sigma$ ) is also compared in Fig. 11c-d with advance ratios. The CSD  $C_P/\sigma$  differs by -5.1 to 4.1% from the CFD  $C_P/\sigma$ . However, there is little change in  $C_P/\sigma$  between the CFD results with and without having the shank area. Therefore, it is concluded that the shank area does not influence the  $C_P/\sigma$  significantly and the primary cause for the unbalanced  $C_P/\sigma$  is not understood.

Figure 12 compares the performance result of the DNW model-scale rotor between the measurement and predictions. The measurement includes the 40x80 full-scale data, although all the predictions are for the DNW model-scale rotor. All three predictions are capable of capturing the trend of the measurement, but their prediction errors vary significantly between the approaches. A larger error occurs near typically the power bucket region ( $\mu=0.14-0.17$ ). The maximum prediction errors are 16.8% for C81 and 7.7% for OVERFLOW. Interestingly, the MSES prediction error is merely 3.3% or less, which is significantly lower than the other two approaches. Since the power is obtained by integrating over the blade span from the blade root cutout to the tip, there would be a small addition (less than 0.7%) to the power if the contribution from the shank area is included in the comprehensive analyses (C81 and MSES). It is worth noting that the power prediction is found sensitive to the  $CFL_{MAX}$  value in the OVERFLOW input. In the present study, the values range from 100 for a low speed to 25 for a high speed.

The power is determined from the shaft torque, which is a sum of the induced ( $i$ ), profile ( $o$ ), and parasite power ( $p$ ) given as below:

$$\begin{aligned} C_P &= C_{P_i} + C_{P_o} + C_{P_p} \\ &= C_{P_i} + C_{P_o} + \mu C_X \end{aligned} \quad (1)$$

The propulsive force coefficient,  $C_X$ , which is a part of parasite drag, is defined positive upstream. Thus, the cruise efficiency,  $L/D_E$  is given in terms of  $C_X$  as follows:

$$\begin{aligned} \frac{L}{D_E} &= \frac{C_L}{(C_{P_i} + C_{P_o}) / \mu} \\ &= \frac{C_L}{C_P / \mu - C_X} \end{aligned} \quad (2)$$

The propulsive force coefficients between the DNW model-scale and NASA AMES 40x80 full-scale tests are compared in Fig. 13a. Since the DNW test was performed in an open jet and the 40x80 test was in the closed section, a correction to the propulsive force is necessary for comparison. So, the DNW wall correction is applied to the 40x80 test data (labeled as 40x80, DNWcorr) in order to match the DNW wall condition. With and without the DNW-wall correction the 40x80 test propulsive forces are shown in the figure. Interestingly, the DNW propulsive force does not agree the corrected 40x80 test data, and the

difference between the two test data becomes larger as the advance ratio increases.

A correlation of the propulsive force coefficients is made in Fig. 13b. All three predictions agree well each other, but display a large gap to the DNW data. Instead, the predictions agree the 40x80 test data. This erroneous behavior in the DNW data appears consistently in the sum of the induced and profile power as well as rotor  $L/D_E$ , as shown in Fig. 14. On the other hand, the MSES results match best the 40x80 data.

### Details of Aeromechanics Behavior

A total power is the global value integrated from all aerodynamic segments along the blade span. Although good performance prediction is made using MSES table lookup, it is not necessary that the MSES result should be accurate locally. To investigate the local aerodynamics behavior, two cruise conditions are chosen: L4 and L7 (see Table 1). The case L4 is adjacent to the minimum power condition, and the L7 is the moderately high speed case at  $\mu=0.32$ .

The contours of  $M^2c_l$ ,  $M^2c_d$ , and  $M^2c_m$  for the L4 case are compared in Fig. 15. There is no significant difference in the contours between the C81, MSES, and OVERFLOW, except for  $M^2c_d$ . So, the difference in  $M^2c_d$  is visualized in Fig. 16 by taking the difference from the MSES result. The difference for the C81 case is found positive almost all over the rotor disk, so using the C81 table gives the power prediction higher than using the MSES, which was expected from Fig. 12. However, the difference for the OVERFLOW case appears much more complex. At  $\mu=0.32$ , similar observations are made in Fig. 17.

Figures 18 and 19 compare  $M^2c_l$ ,  $M^2c_d$ , and  $M^2c_m$  at the 87% span location for  $\mu=0.17$  and  $0.32$ , respectively. The  $M^2c_l$  and  $M^2c_m$  are almost identical between the C81 and MSES, but the MSES  $M^2c_d$  is consistently lower. It is found from the OVERFLOW result that a sharp drop in  $M^2c_d$  is shown on the retreating side for  $\mu=0.17$  but not for  $\mu=0.32$ . Although it shows excellent performance prediction, the MSES is unable to capture the OVERFLOW local characteristic of a sharp drop in drag.

An investigation is made to understand the drop in  $M^2c_d$  by examining the chord force. The nondimensional chord force,  $M^2c_c$  computed by OVERFLOW is plotted in Fig. 20 for  $r/R=0.80-0.95$  at  $\mu=0.17$ . Note that the chord force is positive toward the leading edge. The  $M^2c_c$  displays a sharp drop on the retreating side which is similar to that in  $M^2c_d$ , and

the lowest peak occurs at  $r/R=0.87-0.91$ . The characteristic of OVERFLOW  $M^2c_d$  seems to inherit from the chord force.

A further investigation for  $M^2c_d$  is made with advance ratios. Figure 21 compares the OVERFLOW  $M^2c_d$  at  $r/R=0.87$  for  $\mu=0.09-0.32$ . As expected, a sharp drop is seen on the retreating side, but the peak magnitude depends on the advance ratio. The largest peak occurs at  $\mu=0.14-0.17$  near the power bucket, where a minimum power is required. Interestingly, the peaks shift slowly downstream as  $\mu$  increases, and fades away.

The 3-dimensional rotation effect on the boundary layer could produce a delay of flow separation or stall, particularly for the inboard sections of rotating blades [21]. Separated flow on the airfoil surface stretches outward in the radial direction due to a centrifugal loading, which would result in thinner boundary layer thickness, delay in flow separation, and spanwise flow. This phenomenon may become more dominant on the retreating side due to a low dynamic pressure. The drop in  $M^2c_d$  on the retreating side may be linked with the 3-dimensional rotation effect, which is a shortcoming in capability of any comprehensive analysis.

The predicted trim controls are compared in Fig. 22 at  $\mu=0.17$  and  $0.32$ . As expected, the trim controls are very close between the C81 and MSES cases, and the O2/CII trim controls are slightly different within 0.6 degrees. But, the DNW trim data seems slightly more different especially for the collective control - a difference of 1.3 degrees compared with the MSES result. Blade flap response and elastic twist at the tip are also compared in Figs. 23 and 24 at  $\mu=0.17$  and  $0.32$ . No surprise is found for flap deformations at both advance ratios. But, for the elastic twist the mean of the O2/CII case is lower by 0.55 degrees at  $\mu=0.17$  than the MSES case.

### CONCLUDING REMARKS

An improvement in Bo105 model rotor performance prediction has been successfully made by coupling of unsteady and three-dimensional OVERFLOW 2 CFD aerodynamics solutions into CAMRAD II and using MSES-based table lookup in the CAMRAD II comprehensive analysis.

Three approaches were used for performance prediction: CAMRAD II with the C81 table lookup, CAMRAD II with the MSES-based table lookup, and OVERFLOW-2/CAMRAD II coupling. The prediction errors varied significantly between the analyses, and a

larger error occurred mostly near the power bucket region. The maximum prediction errors in a full sweep of speed were 16.8% for the C81, and 7.7% for the OVERFLOW, but the error was merely 3.3% for the MSES.

The MSES  $M^2 c_d$  was consistently lower compared with the C81 result, which helped the MSES to obtain excellent performance prediction. The table lookup that was constructed at accurate Reynolds numbers as well as Mach numbers using MSES enabled the comprehensive analysis to significantly improve rotor performance prediction.

Although it showed an excellent performance prediction, the CAMRAD II with the MSES-based table lookup was unable to capture the local characteristic of drag displayed by the OVERFLOW. This may be due to a lack of the adequate 3-dimensional aerodynamic capability in the comprehensive analysis.

#### ACKNOWLEDGEMENTS

The Bo105 rotor data was a product of the U.S. Army/German Memorandum of Understanding on Cooperative Research in the field of Helicopter Aeromechanics. The author would like to acknowledge Deutsches Zentrum für Luft- und Raumfahrt e.V. (DLR) in Germany and Duits-Nederlandse Wind Tunnel (DNW) in Netherlands for the DNW Bo105 model-scale test data which is available by means of publication. The author wishes to thank Mr. Thomas H. Maier, AFDD and Mr. Randall L. Peterson, NASA Ames Research Center for their encouragement and knowledge about the test data. The author also likes to acknowledge Dr. Wayne Johnson, NASA Ames Research Center, for his insightful support for CAMRAD II, Mr. Mark Potsdam, AFDD for OVERFLOW, and Dr. Berend van der Wall, DLR, for sharing the resources of NACA 23012 airfoil data.

#### REFERENCES

<sup>1</sup> Langer, H. L., Peterson, R. L., and Maier, T. H., "An Experimental Evaluation of Wind Tunnel Wall Correction Methods for Helicopter Performance," Proceedings of the American Helicopter Society 52nd Annual Forum, Washington, D. C., June 4-6, 1996.

<sup>2</sup> Peterson, R. L., Maier, T., Langer, H. J., and Tränapp, N., "Correlation of Wind Tunnel and Flight Test Results of a Full-Scale Hingeless Rotor," Proceedings of the American Helicopter Society Aeromechanics Specialists Conference, San Francisco, California, January 19-21, 1994.

<sup>3</sup> Langer, H. J., and Tränapp, N., "BO105 Flight Test Data for a Wind Tunnel Test Program," DLR IB 111-93/58, Braunschweig, Germany, September, 1993.

<sup>4</sup> Johnson, W., "Influence of Wake Models on Calculated Tiltrotor Aerodynamics," American Helicopter Society Aerodynamics, Acoustics, and Testing and Evaluation Technical Specialists Meeting Proceedings, San Francisco, CA, January 2002.

<sup>5</sup> Lim, J. W., Nygaard, T. A., Strawn, R., and Potsdam, M., "Blade-Vortex Interaction Airloads Prediction Using Coupled Computational Fluid and Structural Dynamics," *Journal of the American Helicopter Society*, Vol. 52, (4), October 2007, pp. 318-328.

<sup>6</sup> Drela, M., "Newton Solution of Coupled Viscous/Inviscid Multi-element Airfoil Flows," AIAA paper No. 90-1470, Proceedings of 21<sup>st</sup> Fluid, Dynamics, Plasma Dynamics, and Lasers Conference, Seattle, WA, June 1990.

<sup>7</sup> Greer, D., Hamory, P., Krake, K., and Drela, M., "Design and Prediction for a High-Altitude (Low-Reynolds Number) Aerodynamic Flight Experiment," NASA TM-1999-206579, July 1999.

<sup>8</sup> Buning, P., "Consolidation of Time-Accurate, Moving Body Capabilities in OVERFLOW," 6th Overset Composite Grid and Solution Technology Symposium Proceedings, Ft. Walton Beach, Florida, October 8-10, 2002.

<sup>9</sup> Buning, P., G., Gomez, R. J., and Scallion, W. I., "CFD Approaches for Simulation of Wing-Body Stage Separation," AIAA 2004-4838, 22nd AIAA Applied Aerodynamics Conference Proceedings, Providence, RI, August 2004.

<sup>10</sup> Nichols, R. H., Tramel, R. W., Buning, P. G., "Evaluation of Two High-Order Weighted Essentially Nonoscillatory Schemes," *AIAA Journal*, Vol. 46, No. 12, December 2008, pp. 3090-3102.

<sup>11</sup> Lim, J. W., "Summary of NACA 23012 mod Application to HART II Blade," AFDD, USA, July 20, 2001.

<sup>12</sup> Lim, J. W., Tung, C., Yu, Y. H., Burley, C. L., Brooks, T. F., Boyd, D., van der Wall, B. G., Schneider, O., Richard, H., Raffel, M., Beaumier, P., Delrieux, Y., Pengel, K., and Mercker, E., "HART II: Prediction of Blade-Vortex Interaction Loading," 29th European Rotorcraft Forum Proceedings, Friedrichshafen, Germany, September 16-18, 2003.

<sup>13</sup> Staley, J. A., "Validation of Rotorcraft Flight Simulation Program through Correlation with Flight

Data for Soft-in-Plane Ingeless Rotors,” USAAMRDL-TR-75-50, Jan. 1976.

<sup>14</sup> Althaus, D., and Wortmann, F. X., “Experimental Results from the Laminar Wind Tunnel of the Institut für Aero- und Gasdynamik der Universität Stuttgart,” Stuttgarter Profilkatalog I, Friedr. Vieweg & Sohn, Braunschweig, 1981.

<sup>15</sup> Jacobs, E. N., and Clay, W. C., “Characteristics of the N. A. C. A. 23012 Airfoil from Tests in the Full-scale and Variable-Density Tunnels,” NACA TR 530, March 1935.

<sup>16</sup> Loftin, L. K., and Smith, H. A., “Aerodynamic Characteristics of 15 NACA Airfoil Sections at Seven Reynolds Numbers from  $0.7 \times 10^6$  to  $9.0 \times 10^6$ ,” NACA TN 1945, October 1949.

<sup>17</sup> Racisz, S. F., “Effects of Independent Variations of Mach Number and Reynolds Number on the Maximum Lift Coefficients of Four NACA 6-Series Airfoil Sections,” NACA TN 2824, November 1952.

<sup>18</sup> Leishman, J. G., “Dynamic Stall Experiments on the NACA 23012 Aerofoil,” *Experiments in Fluids*, Vol. 9, 1990, pp. 49-58.

<sup>19</sup> Lasuaskas, E., Lutz, T., and Dietz, M., “Influence of Trailing Edge Tab on Moment Characteristics of NACA 23012 Airfoil,” *Aviation*, Vol. XI, no. 4, 2007, pp. 3-8.

<sup>20</sup> Romander, E., Norman, T. R., and Chang, I., “Correlating CFD Simulation with Wind Tunnel Test for the Full-Scale UH-60A Airloads Rotor,” Proceedings of the American Helicopter Society 67th Annual Forum, Virginia Beach, Virginia, May 3-4, 2011.

<sup>21</sup> Corrigan, J.J., and Schillings, J. J., “Empirical Model for Stall Delay Due to Rotation,” American Helicopter Society Aeromechanics Specialists Conference, San Francisco, California, January 1994.

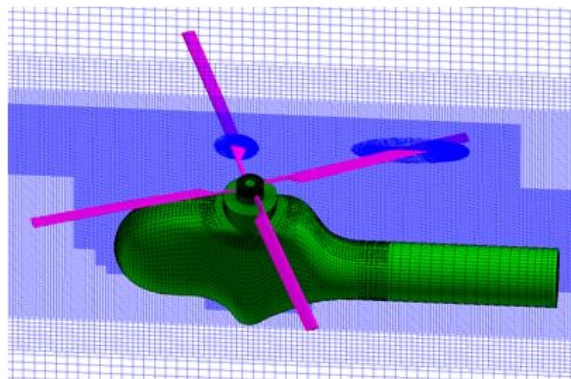


Figure 1. Bo105 fuselage surface grids with a cut through the off-body volume grids.

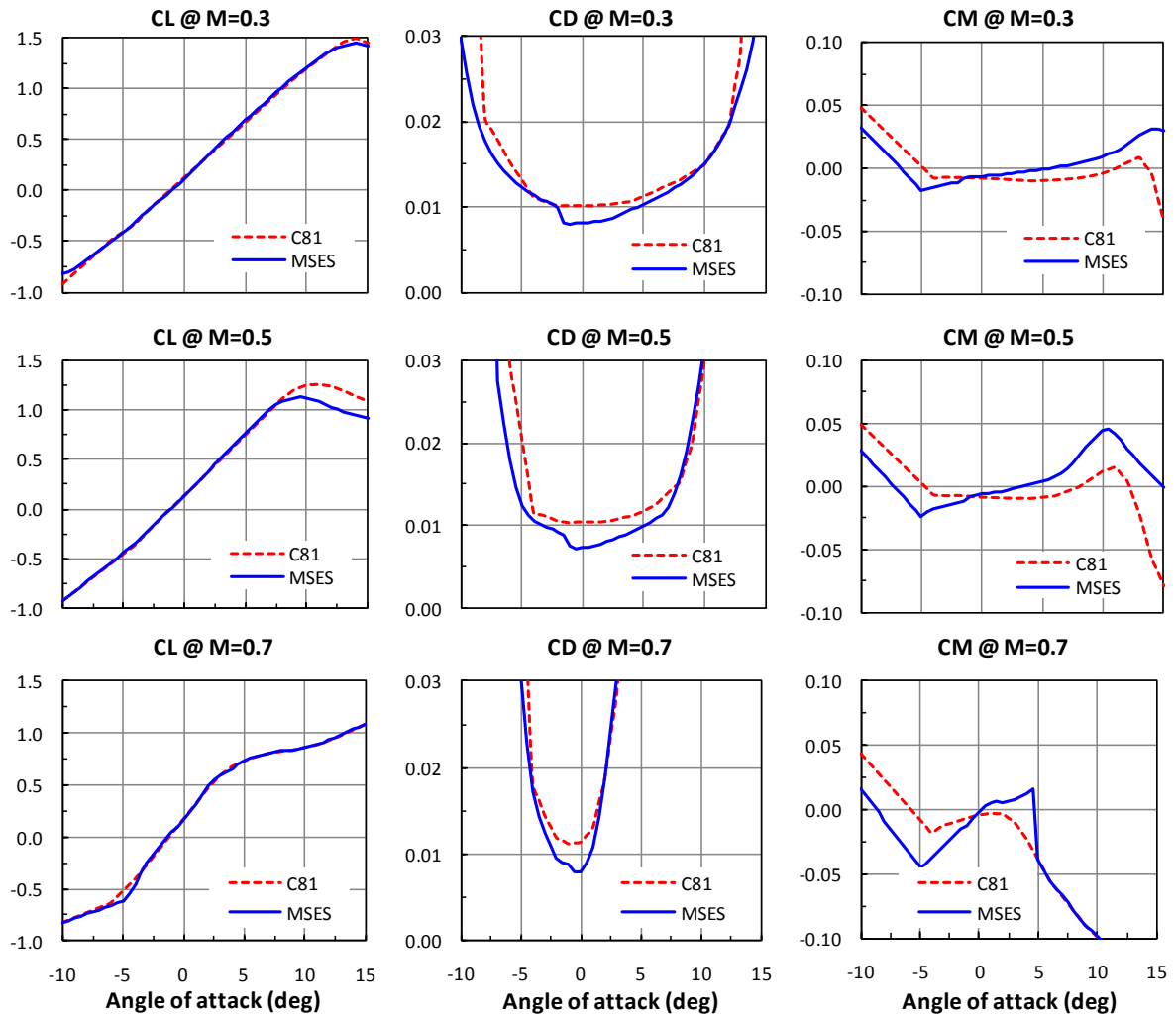


Figure 2. Lift, drag, and pitching moment coefficients between the C81 table and MSES data at  $M = 0.3, 0.5,$  and  $0.7$ .

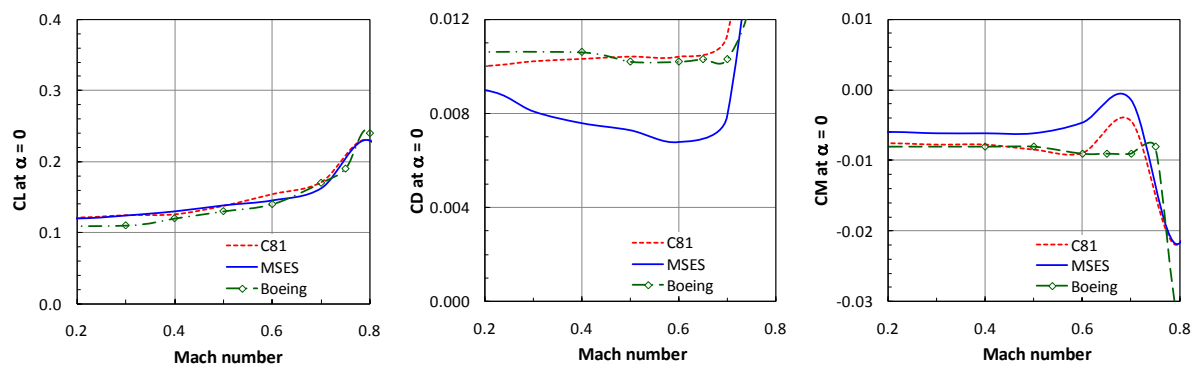


Figure 3. Zero-angle-of-attack lift, drag, and pitching moment coefficients between C81, MSES, and Boeing data.

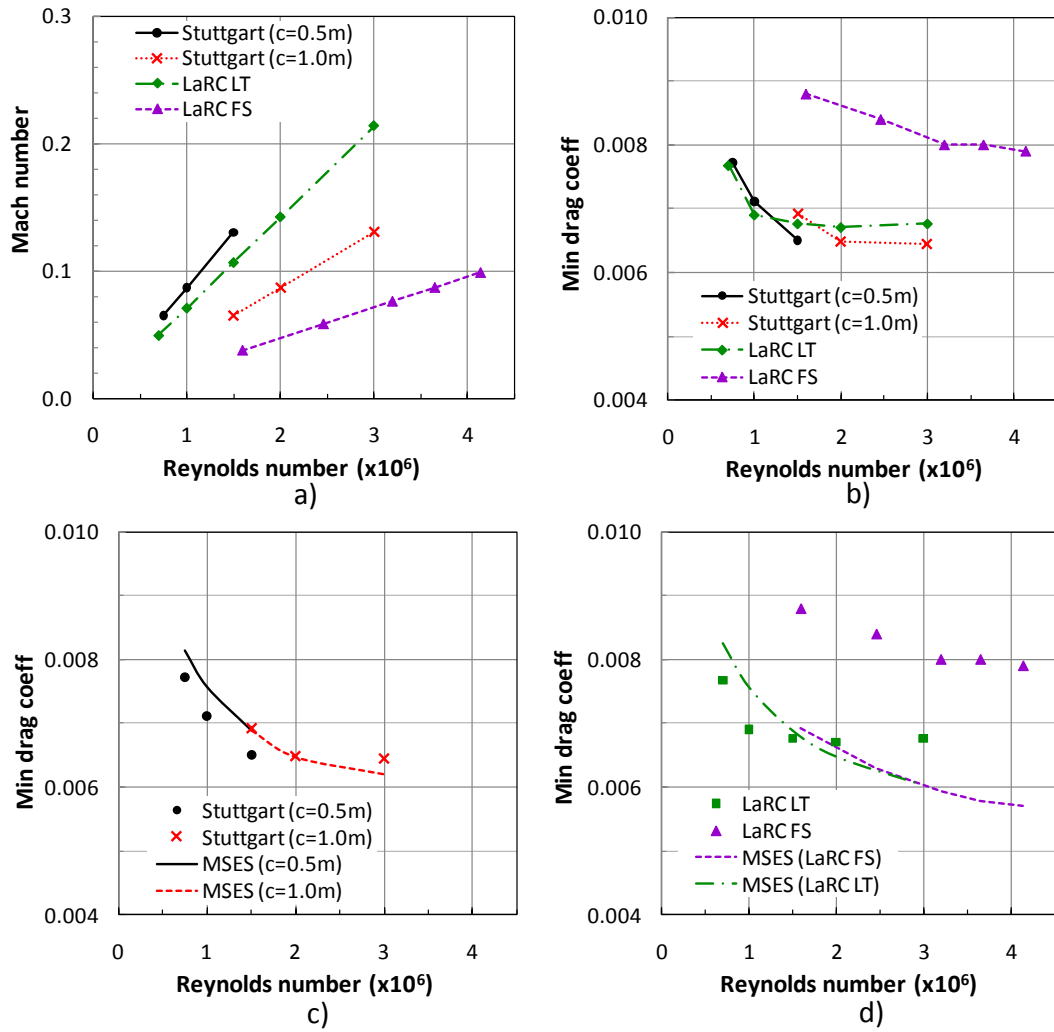


Figure 4. Correlations of Mach numbers and minimum profile drag coefficients for NACA 23012 airfoil: a) Mach numbers, b) measured minimum drag, c) Stuttgart data vs. MSES, d) LaRC data vs. MSES.

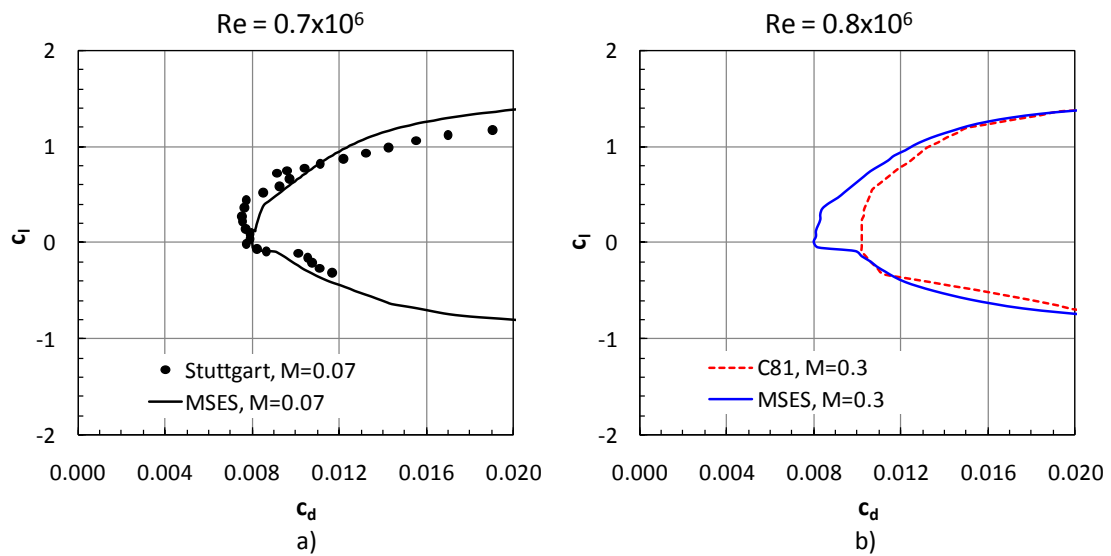


Figure 5. Drag polar at Reynolds number of  $0.7 \times 10^6$ : a)  $M=0.07$ , b)  $M=0.3$ .

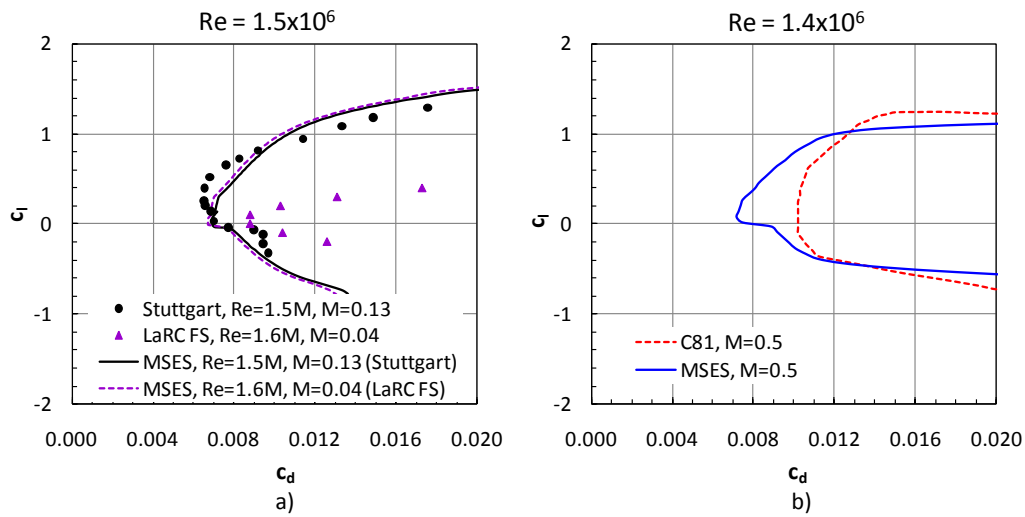


Figure 6. Drag polar at Reynolds number of  $1.5 \times 10^6$ .

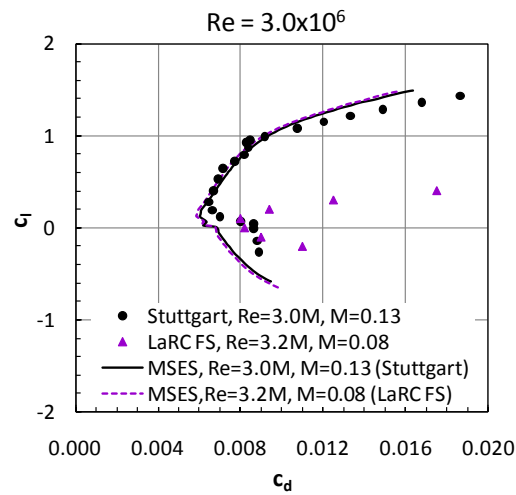


Figure 7. Drag polar at Reynolds number of  $3.0 \times 10^6$ .

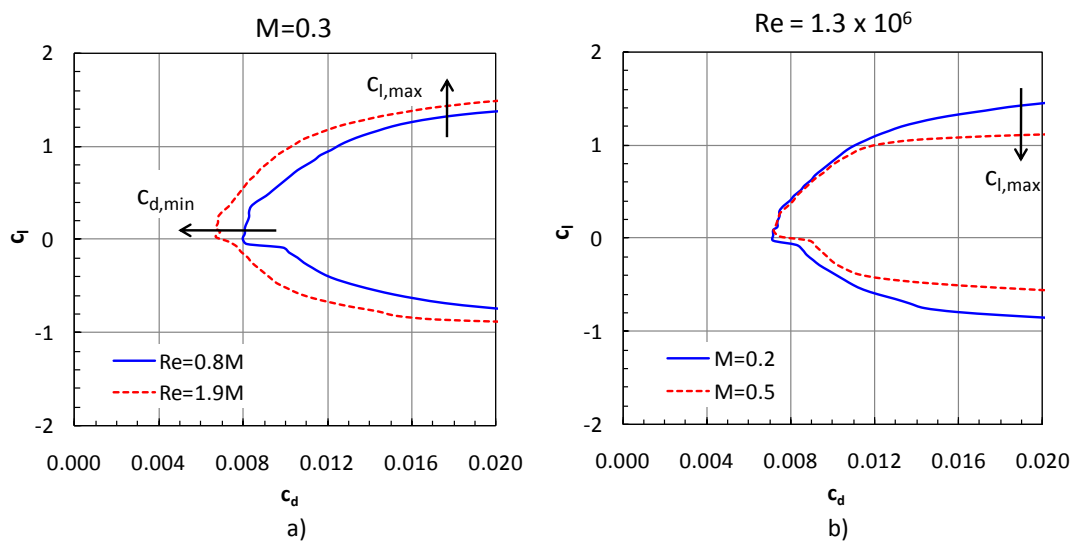


Figure 8. Effect of Reynolds number and Mach number on drag polar: a) Reynolds number, b) Mach numbers.

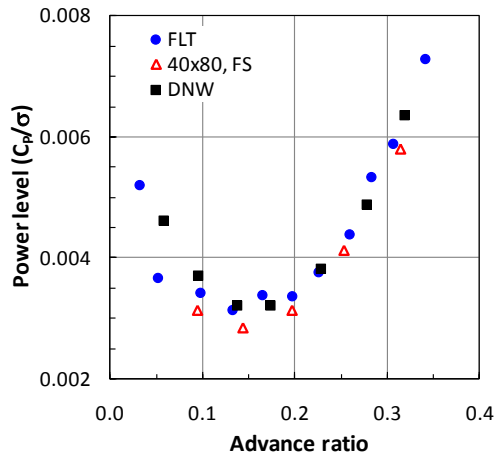


Figure 9. Power level ( $C_p/\sigma$ ) of Bo105 rotor in cruise for flight test, NASA AMES 40x80 full-scale test, and DNW model-scale test.

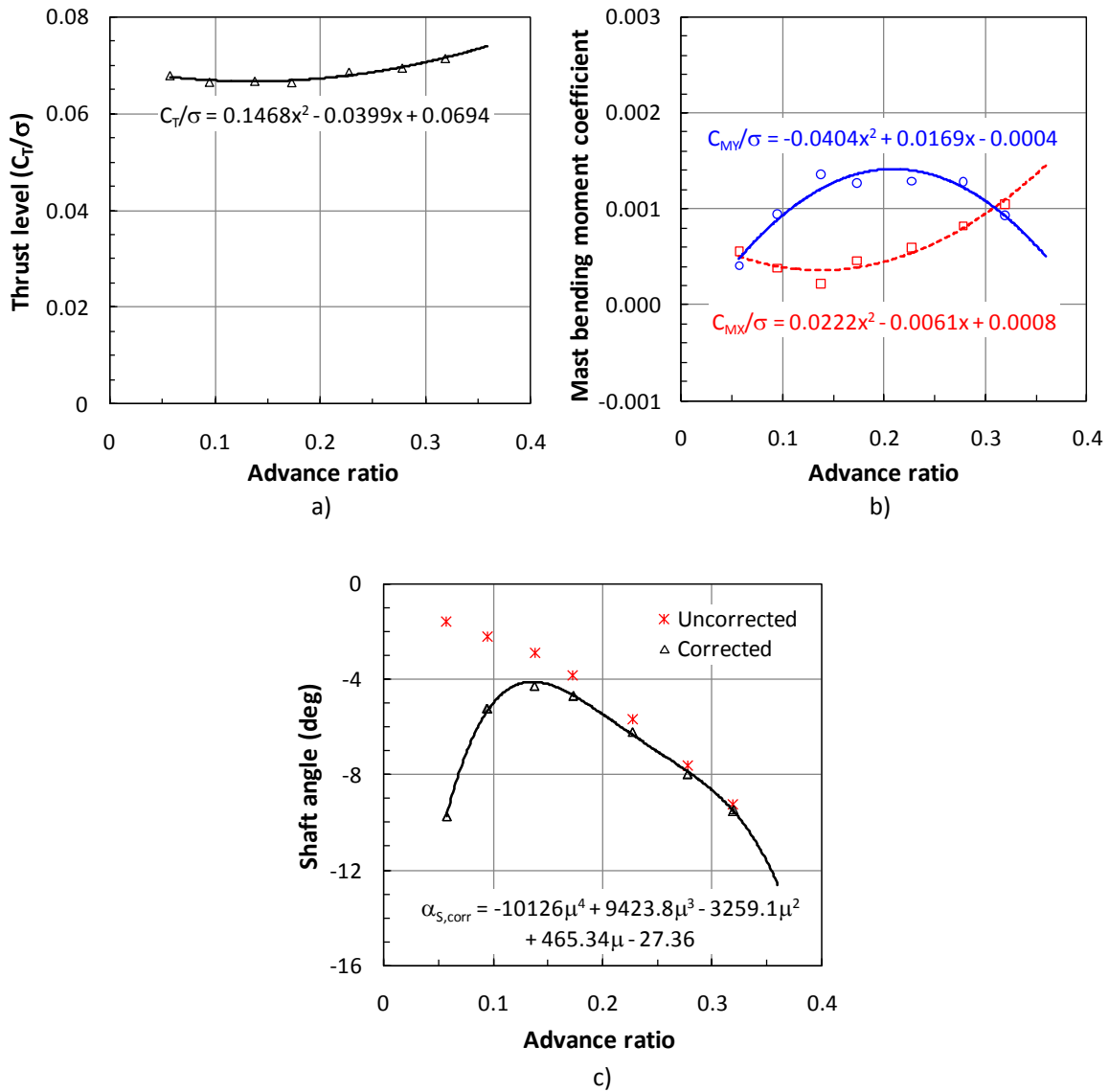


Figure 10. Measured trim target and shaft angle in the DNW test: a) thrust level ( $C_T/\sigma$ ), b) shaft roll ( $C_{MX}/\sigma$ ) and pitching moment ( $C_{MY}/\sigma$ ), c) shaft angle.

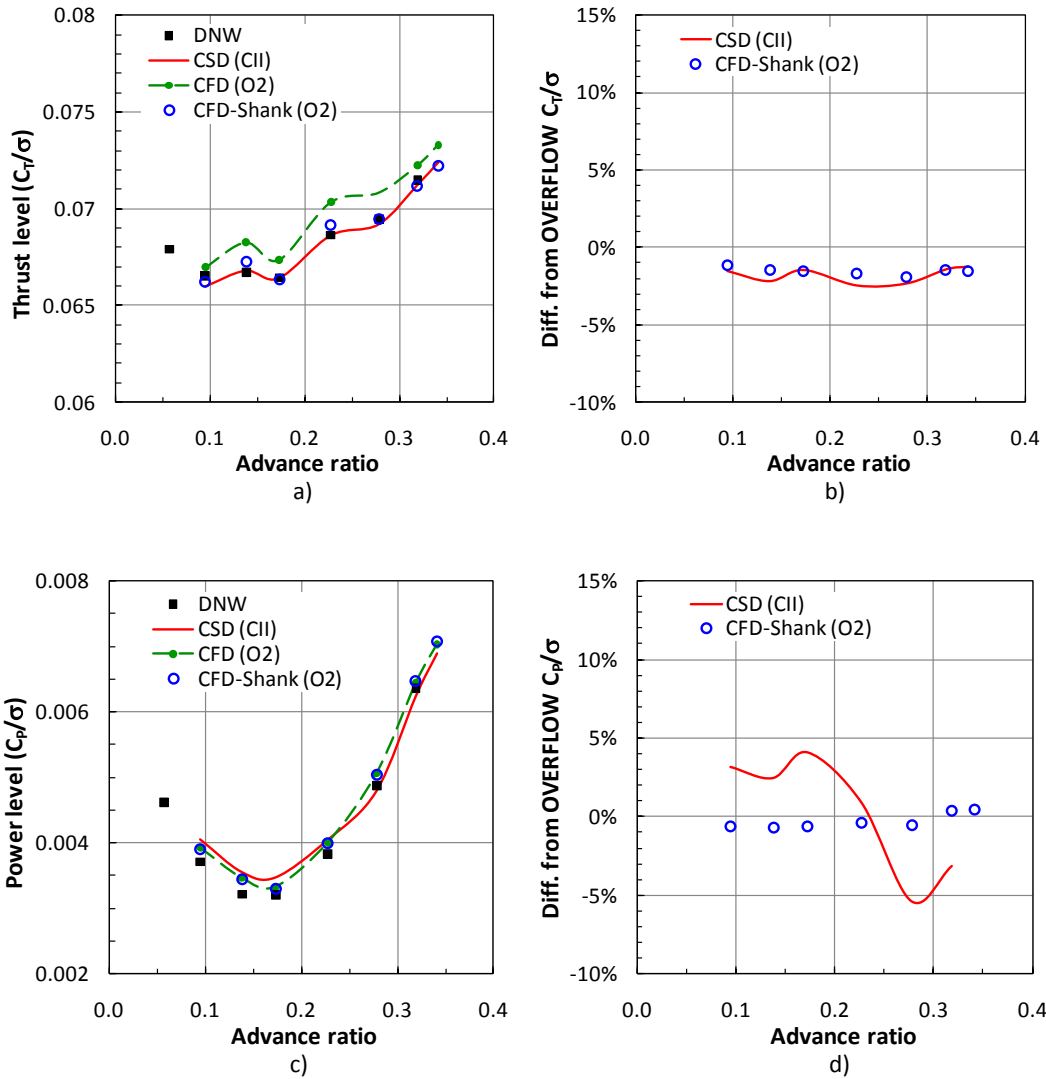


Figure 11. Comparison of the predicted thrust and power level for the DNW test data between the CSD (CAMRAD II) and CFD (OVERFLOW) analyses: a) thrust level ( $C_T/\sigma$ ), b) thrust difference from the OVERFLOW prediction, c) power level ( $C_P/\sigma$ ), d) power difference from the OVERFLOW prediction.

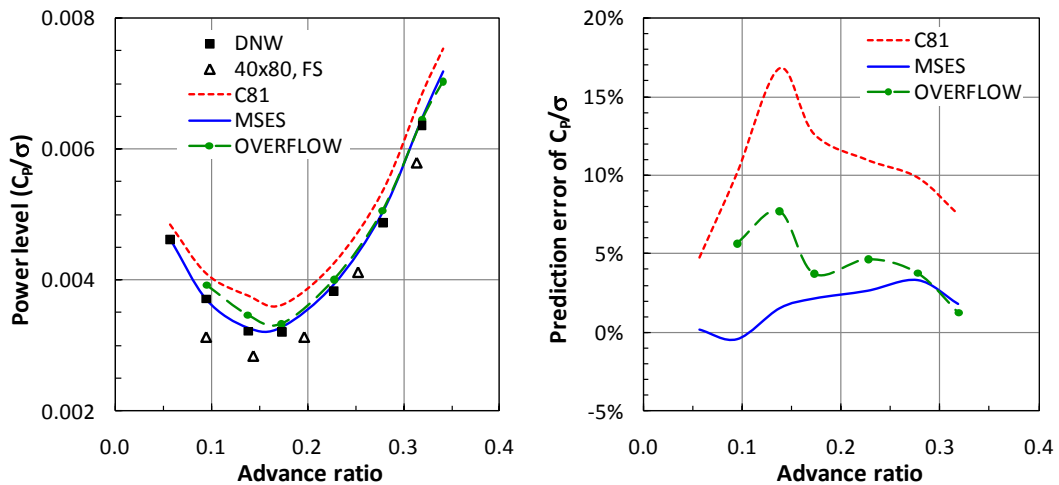


Figure 12. Performance comparison for the Bo105 model rotor between the measurement and predictions.

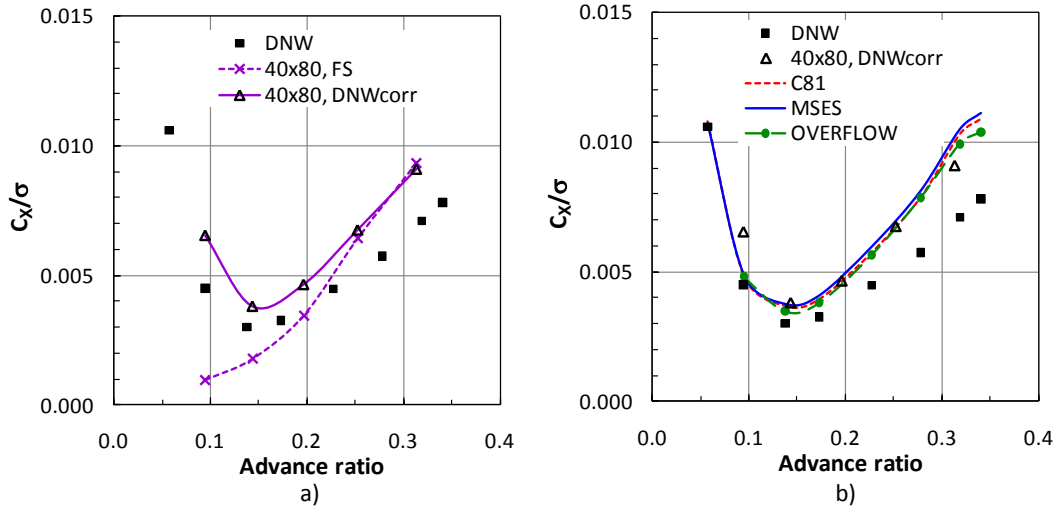


Figure 13. Comparison of propulsive force coefficients for the Bo105 model rotor: a) with and without DNW wall correction, b) all corrected with the DNW wall correction.

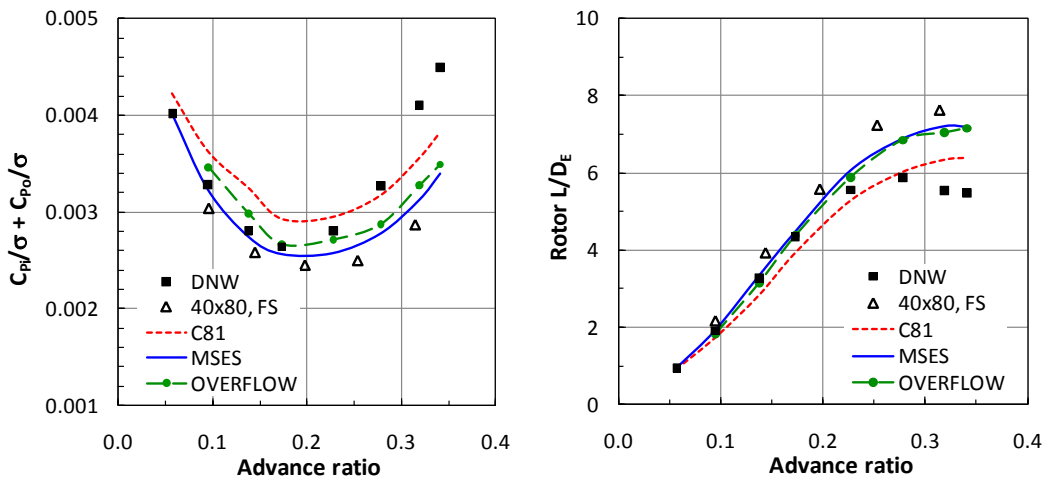


Figure 14. Comparison of the sum of the induced and profile power coefficient, and the cruise efficiency for the Bo105 model rotor.

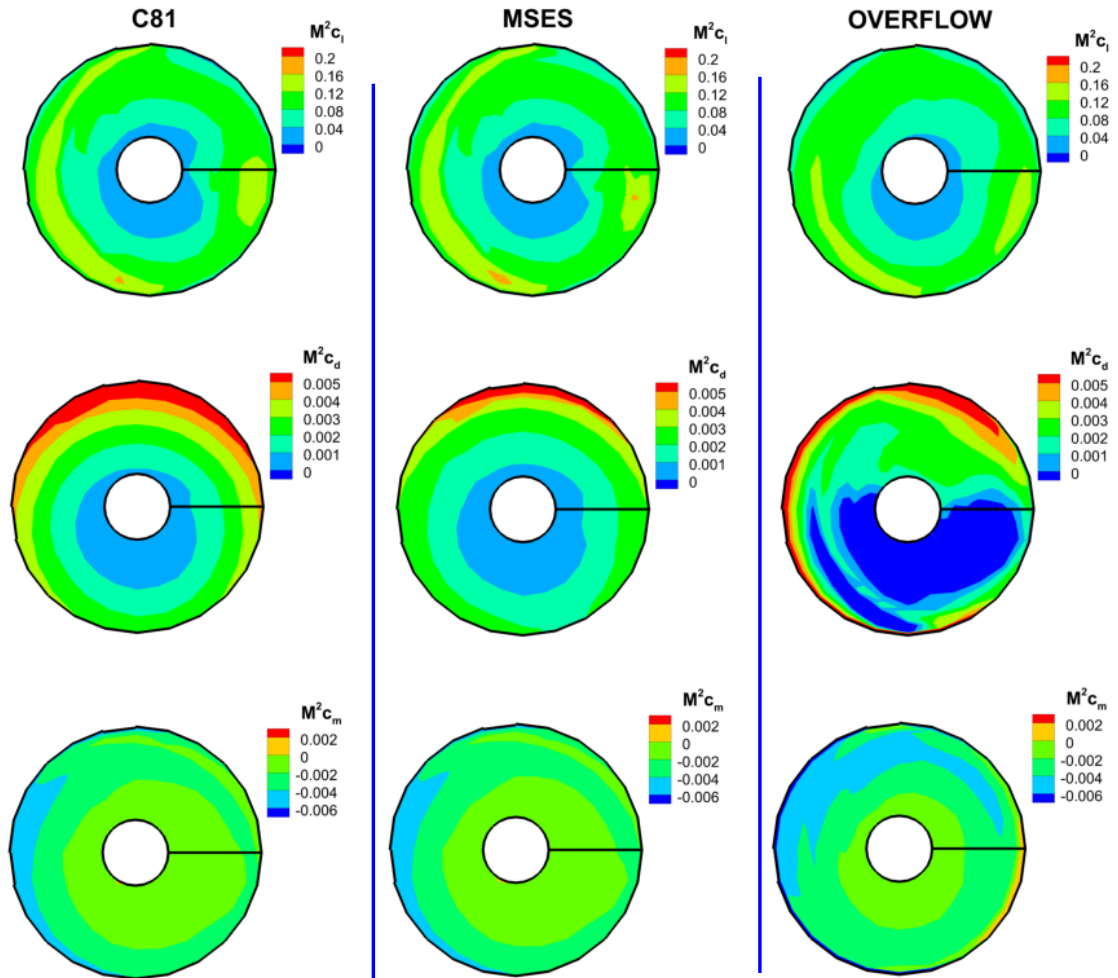


Figure 15. Comparison of  $M^2 c_l$ ,  $M^2 c_d$ , and  $M^2 c_m$  at  $\mu=0.17$  (case L4) between the C81, MSES, and OVERFLOW cases.

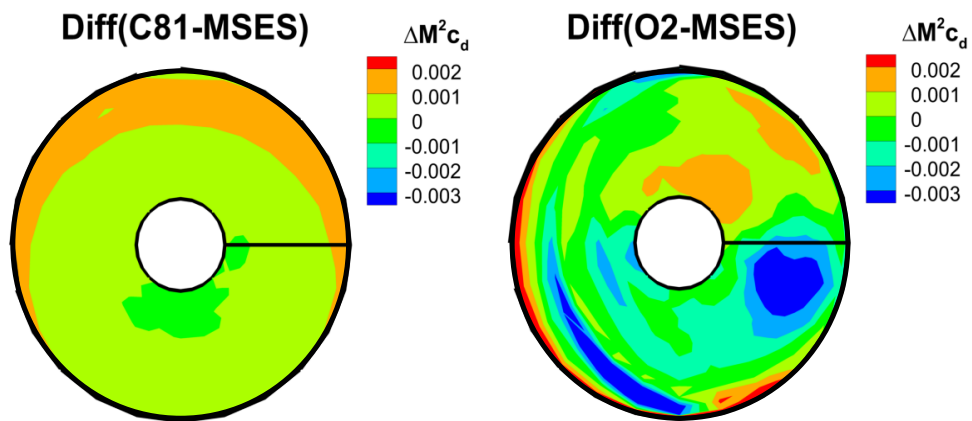


Figure 16. Comparison of the difference in  $M^2 c_d$  at  $\mu=0.17$  (case L4), referenced from the MSES result.

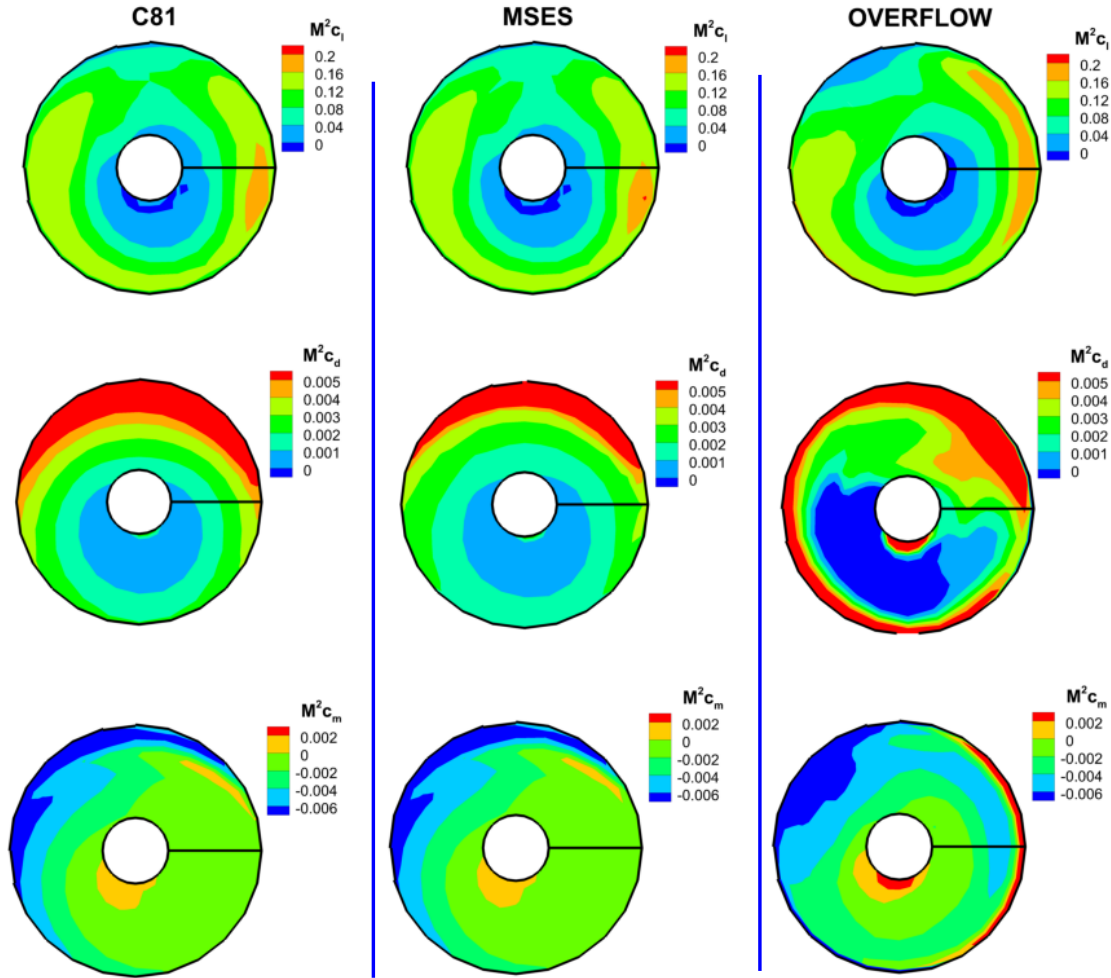


Figure 17. Comparison of  $M^2 c_l$ ,  $M^2 c_d$ , and  $M^2 c_m$  at  $\mu=0.32$  (case L7) between the C81, MSES, and OVERFLOW cases.

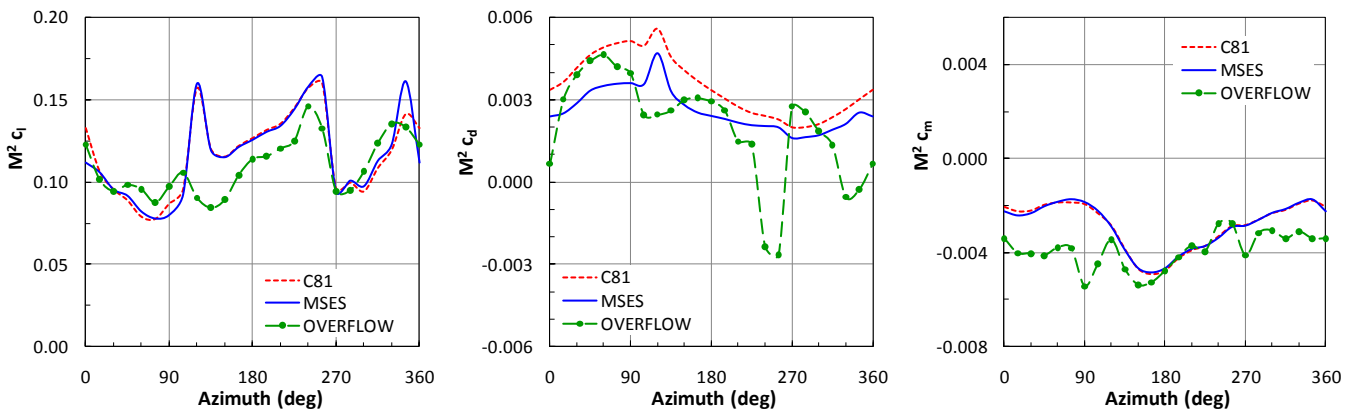


Figure 18. Comparison of  $M^2 c_l$ ,  $M^2 c_d$ , and  $M^2 c_m$  at the 87% span location for  $\mu=0.17$  (case L4).

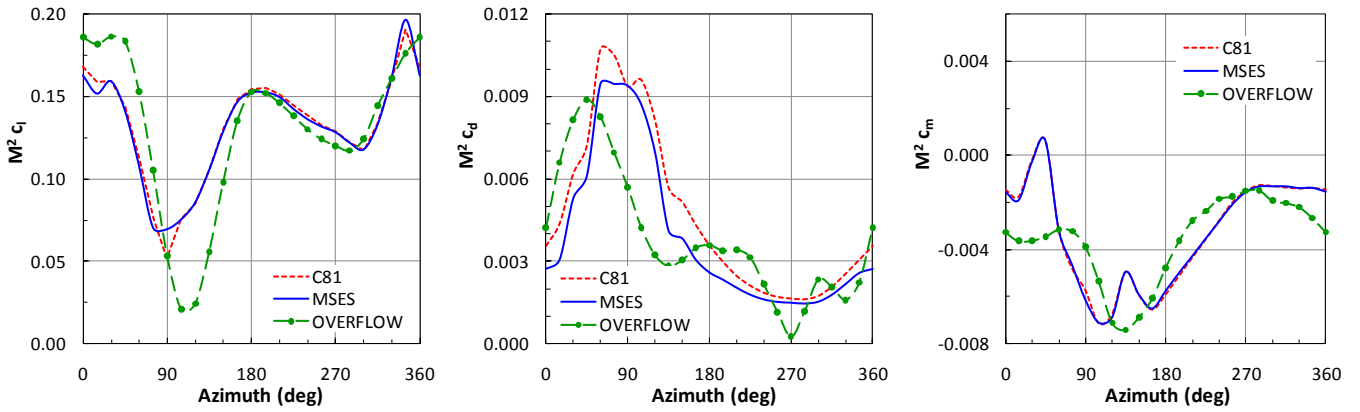


Figure 19. Comparison of  $M^2 c_l$ ,  $M^2 c_d$ , and  $M^2 c_m$  at the 87% span location for  $\mu=0.32$  (case L7).

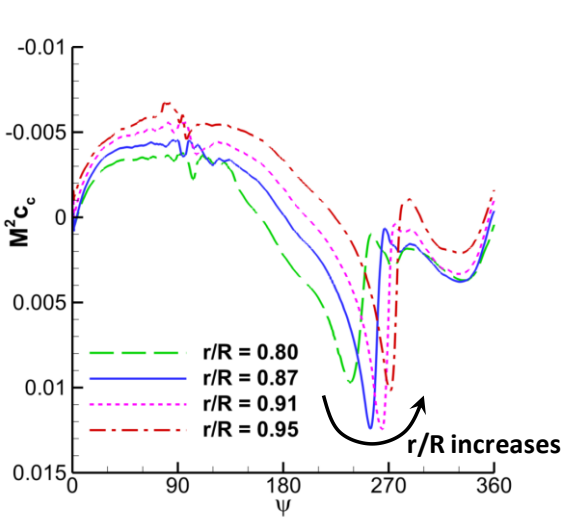


Figure 20. Spanwise comparison of the OVERFLOW  $M^2 c_c$  at  $\mu=0.17$  (case L4).

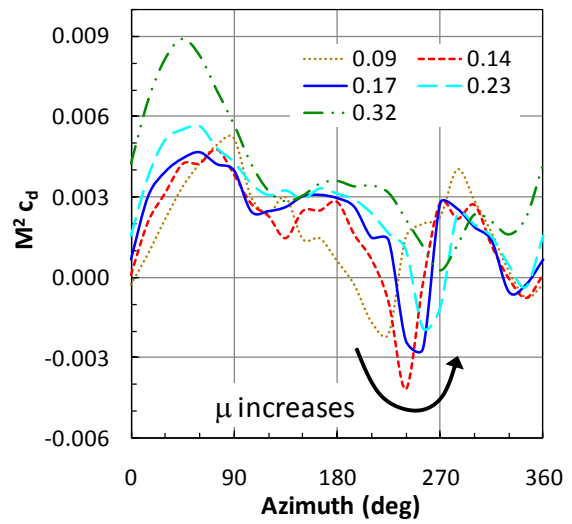


Figure 21. Comparison of the OVERFLOW  $M^2 c_d$  at  $r/R=0.87$ .

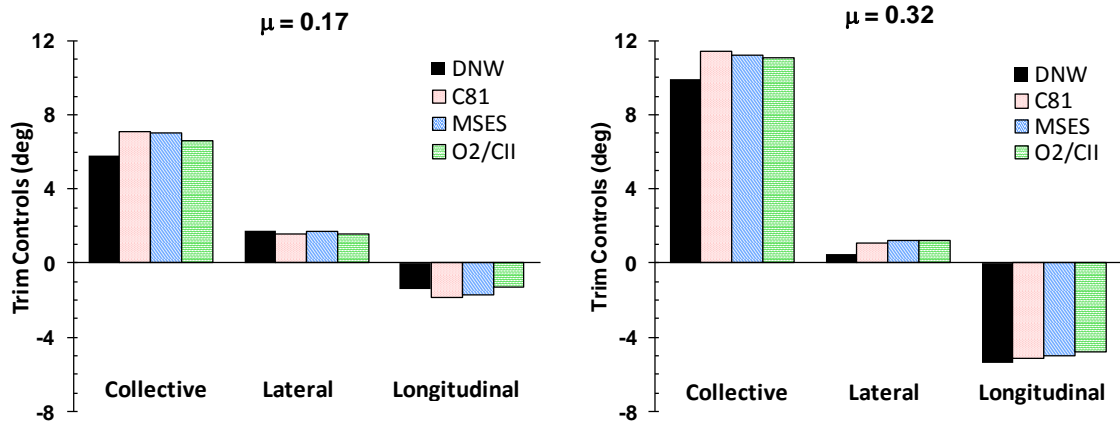


Figure 22. Comparison of trim controls between the C81, MSES, and O2/CII cases at  $\mu=0.17$  (case L4) and  $0.32$  (case L7).

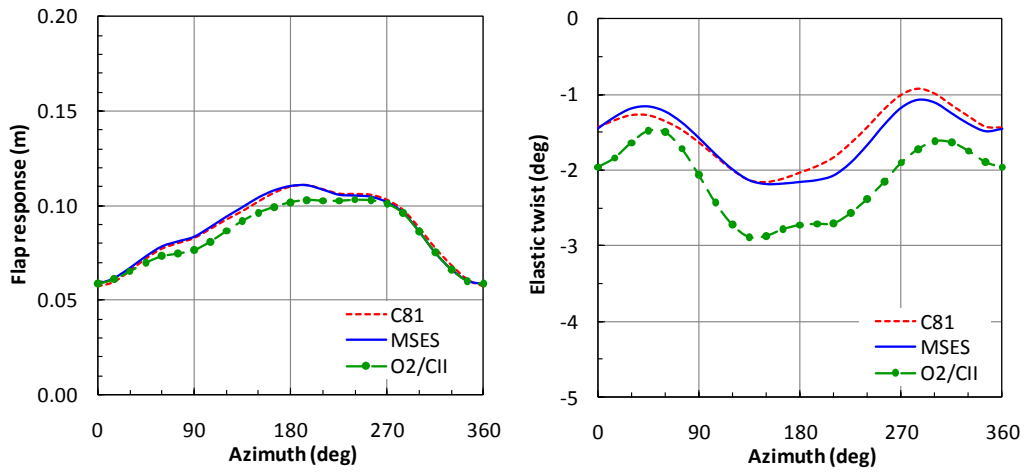


Figure 23. Comparison of blade flap response and elastic twist at the tip for  $\mu=0.17$  (case L4).

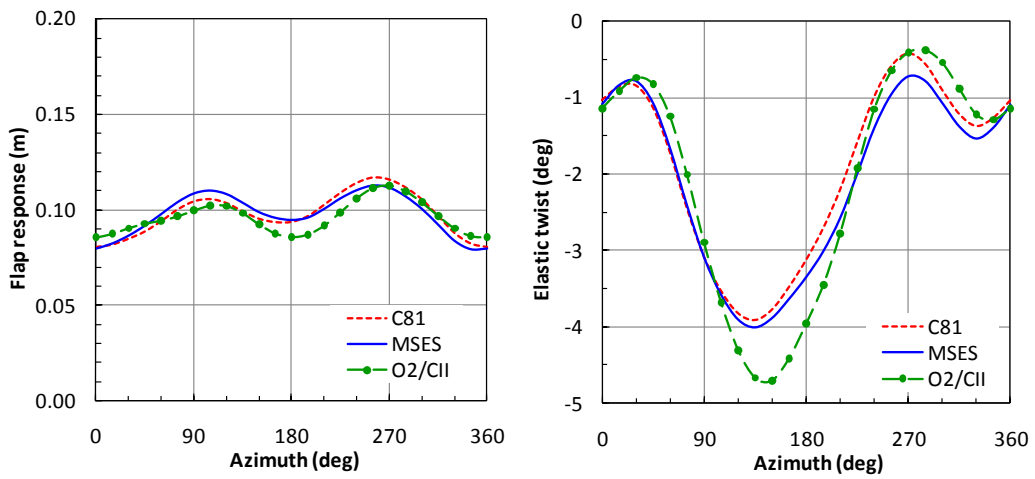


Figure 24. Comparison of blade flap response and elastic twist at the tip for  $\mu=0.32$  (case L7).